



An efficient strategy for the partial oxidation of methane into methanol over POM-immobilized MOF catalysts under ambient conditions

Taikang Jia ^{a,b,1}, Wenjing Wang ^{a,b,1}, Ling Zhang ^{a,*}, Di Zeng ^{a,b}, Juxue Wang ^{a,b}, Wenzhong Wang ^{a,b,c,**}

^a State Key Laboratory of High Performance Ceramics and Superfine Microstructure, Shanghai Institute of Ceramics, Chinese Academy of Sciences, Shanghai 200050, China

^b Center of Materials Science and Optoelectronics Engineering, University of Chinese Academy of Sciences, Beijing 100049, China

^c School of Chemistry and Materials Science, Hangzhou Institute for Advanced Study, University of Chinese Academy of Sciences, Hangzhou 310024, China



ARTICLE INFO

Keywords:

Dark photocatalysis
Hydrocarbons
Oxidation
Selectivity
EPR

ABSTRACT

One of the scientific obstacles in the direct conversion of methane to methanol lies in how to improve product selectivity. A dark photocatalysis mode that decouples solar energy in the dark may effectively alleviate this challenge. Herein, a range of composites had been prepared in which Fe-BTC was employed as the gas enrichment unit, while phosphotungstic acid (PTA) acted mainly as an electron storage within the framework. The modified reaction system allowed for the achievement of methanol yields up to $968 \mu\text{mol}\cdot\text{g}_{\text{cat}}^{-1}\cdot\text{h}^{-1}$ under ambient conditions. Besides extrinsic factors, such as a gentle reaction environment and avoidance of the oxidation reactions between photogenerated holes and alcohols, we also demonstrated through *in situ* EPR measurements that the introduced PTA effectively regulated $\bullet\text{OH}$ radicals and suppressed their further reaction with methanol. Moreover, the strategy demonstrated its universality by effectively enhancing the performance of other POM-immobilized MOF composites. This work opens a new path for the efficient and targeted conversion of inert methane to methanol.

1. Introduction

Methane, the primary constituent of natural gas, is a valuable carbon resource, hydrogen storage medium, and greenhouse gas [1,2]. Methanol is a crucial raw material in the industrial sector, as it retains most of the original energy from methane and has emerged as a highly sought-after new energy fuel [3,4]. The direct conversion of methane to methanol (DCMM) is considered a "dream reaction", it represents a revolutionary approach to energy utilization and environmental protection, as well as an exploration of scientific issues related to C₁ chemistry [5]. However, there are significant hurdles during research, particularly in how to improve methanol selectivity and achieve targeted conversion [6,7]. The intrinsic reason for this challenge lies in the higher instability of methanol compared to methane, while the extrinsic reason can be attributed to the difficulty in optimizing input energy configuration in reactions.

Recently, an increasing number of scholars have been striving to achieve efficient DCMM reactions through photocatalysis, as it enables reactions to occur at low or even room temperature, making it highly appealing for methane conversion applications [8,9]. The mild conditions can alleviate the Brownian motion of methane molecules, thereby enhancing their binding to the catalyst surface. Additionally, they effectively retard methanol overoxidation, most critically, reduce process costs while achieving substantial energy savings [10]. Nevertheless, on the one hand, the liquid-phase environment mitigates the tendency of methyl radicals generated from methane activation coupling to ethane, thereby being relatively more favorable for their stabilization. Methanol displays strong interactions with the hydrophilic surface of the catalyst, thus polar solvents (e.g., water) facilitate its further extraction [11,12]. Regrettably, the photocatalytic gas-liquid-solid three-phase reaction is often accompanied by the generation of reactive oxygen species (ROS) such as $\bullet\text{OH}$ and $\bullet\text{O}_2$, whose non-selective characteristics can promote

* Corresponding author.

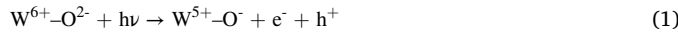
** Corresponding author at: State Key Laboratory of High Performance Ceramics and Superfine Microstructure, Shanghai Institute of Ceramics, Chinese Academy of Sciences, Shanghai 200050, China.

E-mail addresses: lingzhang@mail.sic.ac.cn (L. Zhang), wzwang@mail.sic.ac.cn (W. Wang).

¹ Taikang Jia and Wenjing Wang contributed equally to this work.

methanol overoxidation if not properly controlled [13]. A common strategy in photocatalyst design involves the spatial separation of oxidation and reduction sites (hole/electron traps) to facilitate the separation of photogenerated carriers, while simultaneously improving methanol selectivity by reducing unnecessary collisions between radicals [14,15]. On the other hand, enhancing incident photon energy to facilitate activating methane may lead to extra methanol consumption due to alcohols function as an efficient sacrificial agent for photo-generated holes [16]. Hence, it is worth thinking about developing alternative catalytic strategies to circumvent this paradox. We have been drawn to a novel mode of dark photocatalysis for decoupling solar energy in the absence of light, which involves storing photogenerated electrons produced by the photocatalyst under irradiation and subsequently releasing them in darkness [17]. This approach aims to mitigate the effects of multiple harmful side reactions caused by an excess of active species under irradiation and enhance the efficiency of light energy utilization. Our previous work had shown that amorphous TiO₂ could capture photogenerated electrons (resulting in the conversion of Ti⁴⁺ to Ti³⁺) and extract protons from the sacrificial agent under UV excitation [18]. Upon cessation of light exposure and introduction of 5-hydroxymethylfurfural (HMF), H⁺/e⁻ pairs on the catalyst surface underwent coupling transfer, leading to substrate hydrogenation and ultimately yielding 2,5-bis(hydroxymethyl)furan (BHMF). A remarkably high selectivity (~99 %) was achieved throughout the whole process.

In addition, enhancing the efficient adsorption of methane is a prerequisite for its activation, given its low water solubility. Most metal-organic frameworks (MOFs) with a porous structure possess an enormous specific surface area with excellent permeability, facilitating enriched substrate adsorption and enhancing reactant mass transfer. Imyen et al. designed a e-ZSM-5 @ZIF-8 composite catalyst in which methane can be adsorbed on ZIF-8 at 50 °C and subsequently converted to methanol on Fe-ZSM-5 at 150 °C [19]. This work exemplified the enhanced reaction activity from methane adsorption facilitated by MOFs. Considering the exceptional photostability and water stability of H₃BTC as a framework ligand, Fe-BTC was chosen as the host material in this work, which was also an excellent methane storage material [20]. Further, the polyoxometalates (POMs) were encapsulated as reservoirs for photogenerated electrons, while water served as both a sacrificial agent and a proton source [21,22]. Specifically, phosphotungstic acid (PTA) exhibits a highly excitable ligand-to-metal charge transfer (LMCT) process (O_{2p} → W_{5d}) when exposed to UV irradiation, the holes generated in the O_{2p} orbital possess a high oxidizing ability towards the water, resulting in the self-reduction of PTA (Eqs. 1–3). The advantage of this composite lies in the POMs providing the electron-rich centers, while the MOFs enhance the stability of the reduced POMs. Consequently, it has been attracting increasing attention [23–25].



Herein, we highlighted a series of POM-immobilized MOF host-guest catalysts to validate the possibility of methane to methanol direct conversion via dark photocatalysis. In the presence of hydrogen peroxide as an oxidant under ambient conditions, photogenerated electrons captured by PTA interacted with them in darkness, while metal iron sites on Fe-BTC triggered Fenton-like reactions. The •OH generated in the process activated methane to form •CH₃, which then combined with •OH to produce methanol. This approach effectively reduced the excessive decomposition of hydrogen peroxide and prevented methanol consumption during irradiation. Besides, the electron-rich environment of PTA anion exerted a stabilizing effect on •CH₃ and effectively confined generated •OH on the surface, which enhanced their binding with •CH₃. The synergistic effects of these factors significantly improved the methanol selectivity.

2. Experiment

2.1. Materials

All the chemicals involved were of analytical grade and used without further purification. Phosphotungstic acid hydrate (H₃PW₁₂O₄₀·x H₂O, PTA), Iron(III) nitrate nonahydrate (Fe(NO₃)₃·9 H₂O), Copper(II) nitrate trihydrate (Cu(NO₃)₂·3 H₂O) were purchased from Sinopharm Chemical Reagent Co., Ltd. (Shanghai, China). Tungstosilicic acid hydrate (H₄SiW₁₂O₄₀·x H₂O, STA) was supplied by Macklin Reagent Co., Ltd. (Shanghai, China). Trimesic acid (H₃BTC) was provided by Adamas-beta Reagent Co., Ltd. (Shanghai, China).

2.2. Catalyst preparation

2.2.1. Synthesis of Fe-BTC

Fe-BTC was synthesized on the development of the method previously described in the literature [26]. Briefly, Fe(NO₃)₃·9 H₂O (6 mmol, 2.424 g) and H₃BTC (5 mmol, 1.051 g) were thoroughly mixed with 25 mL of deionized water in a Teflon liner with a volume of 50 mL. After stirring for 30 min, the Teflon liner was sealed inside a stainless-steel autoclave and maintained at 130 °C for 72 h. After the heat treatment, the autoclave was allowed to cool down naturally to room temperature. The precipitated Fe-BTC was then collected and washed with deionized water several times. Finally, the obtained orange powder was freeze-dried for 12 h.

2.2.2. Synthesis of Cu-BTC

Cu-BTC was synthesized via a simple method at room temperature. Briefly, 1 g Cu(NO₃)₂·3 H₂O and 0.9 g H₃BTC were dissolved in 200 mL ethanol. The solution was continuously stirred for 24 h at room temperature until precipitates appeared. The precipitates were collected by centrifugation and washed with ethanol and deionized water. Finally, the obtained blue powder was freeze-dried for 12 h.

2.2.3. Fabrication of PTA/Fe-BTC-X (PWFe-X)

PTA (0.6, 1.2, 1.8 mmol) was introduced into the MOF precursor mixture at molar ratios of PTA to metal species in the material of 0.1:1, 0.2:1, and 0.3:1, respectively. The resulting suspension underwent a procedure identical to that of Fe-BTC synthesis. During the reaction process, PTA clusters were encapsulated within the cavities of Fe-BTC. Following the same collecting process as described above, a series of PTA/Fe-BTC composites were obtained and designated as PWFe-X (X = 1, 2, 3). Besides, PTA/Cu-BTC and STA/Fe-BTC were prepared similarly, and the quantity of POMs added satisfies the requirement of a 0.2:1 molar ratio concerning the corresponding metal species.

2.3. Characterization

Powder X-ray diffraction (XRD) patterns were collected on a Bruker D8 advance X-ray diffractometer with Cu K α radiation. The morphology and size of the samples were observed with scanning electron microscopy (SEM, FEI verios G4 UC). Fourier transform infrared (FTIR) spectra were measured on a Bruker TENSOR 27 spectrometer over 4000–400 cm⁻¹ with a resolution of 4 cm⁻¹. Raman spectroscopy was performed by a Renishaw inVia Raman microscope with a 785 nm excitation laser. The Barret-Joyner-Halenda (BJH) pore size distribution was obtained by Micromeritics 3Flex specific surface and porosity analyzer. X-ray photoelectron spectroscopy (XPS) measurements were examined at a Thermo Fisher ESCALAB 250Xi XPS microprobe using monochromatic Al K α radiation (1253.6 eV) as the X-ray source. UV-vis absorption spectra were recorded by Hitachi U3010 spectrophotometer with BaSO₄ as the reference. The actual content of each element of the samples was determined by inductively coupled plasma optical emission spectroscopy (ICP-OES, Agilent 730). Electron paramagnetic resonance (EPR) spectroscopy was measured on Bruker EMX NANO Desktop

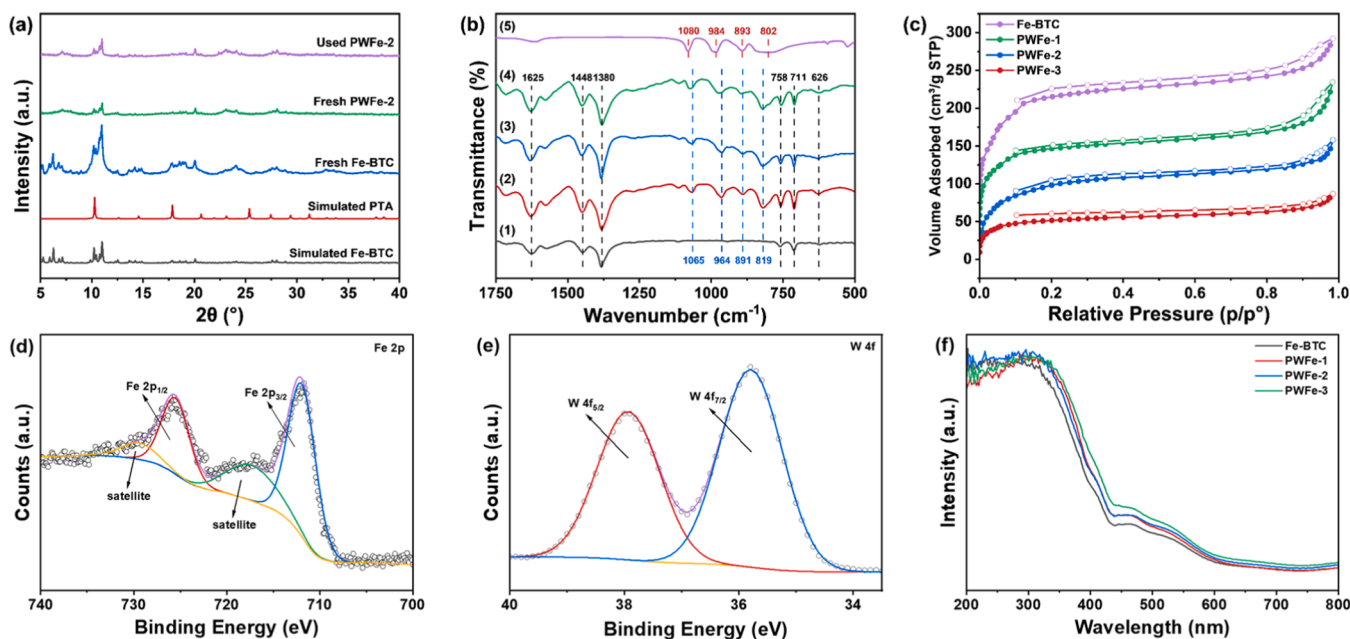


Fig. 1. The characterizations of catalysts. (a) The XRD patterns. (b) IR spectra of (1) Fe-BTC, (2) PWFe-1, (3) PWFe-2, (4) PWFe-3 and (5) PTA. (c) The N_2 adsorption-desorption isotherms at 77 K. High-resolution XPS spectra of (d) Fe 2p and (e) W 4f for PWFe-2. (f) Ultraviolet-visible absorption spectra.

electron paramagnetic resonance spectrometer.

Photocurrent testing was conducted on a Chenhua CHI 660D electrochemical workstation with a standard three-electrode quartz cell system. A 365 nm LED was used as the light source. Platinum sheet and Ag/AgCl electrode were used as counter electrode and reference electrode, respectively. Fluorine-doped tin oxide (FTO) glass coated with photocatalysts was used as the working electrode. In detail, 10 mg photocatalysts were dispersed into 1 mL ethanol solution, and 5 μL 5 % Naion reagent was added. The mixture was ultrasonically scattered for 20 min 100 μL mixture was spread evenly onto the FTO glass, and then the FTO glass was dried. 0.5 M Na_2SO_4 ($\text{pH} = 6.8$) was used as the electrolyte solution.

2.4. Performance experiments

The evaluation of the catalysts was conducted in a 300 mL homemade glass reactor equipped with a quartz window at the top. The reaction system was maintained at 25 °C by circulating water throughout the process. Typically, 15 mg catalysts were dispersed in 30 mL of deionized water and transferred into the reactor, where they remained suspended by mechanical stirring. Light irradiation was carried out under a 365 nm LED lamp (30 W) for 30 min while nitrogen gas was continuously bubbled through the suspension to remove air from the reactor and oxygen produced by the light reaction. After switching off the lamp, a mixture of CH_4 (10 %) and N_2 (90 %) with a gas flow rate of 150 mL/min was introduced, along with a specific amount of H_2O_2 or O_2 added to the suspension, which reacted for 1 h. Finally, 4 mL of liquid was extracted from the reactor and filtrated through a Millipore filter with a pore size of 0.22 μm to remove catalysts for detecting liquid products. Specifically, CH_3OH and $\text{C}_2\text{H}_5\text{OH}$ in solution were analyzed using gas chromatography (GC7900, Tianmei) equipped with the flame ionization detector (FID) through a SE-54 column. It was worth noting that the hydrogen peroxide present in the solution may have a corrosive impact on the column, requiring attention to its reliability and longevity. The HCOOH obtained after the reaction was analyzed by high-performance liquid chromatography (HPLC, Agilent 1260) equipped with a C18 column and a UV detector. The mobile phase consisted of acetonitrile (chromatographic purity) and an H_3PO_4 solution adjusted to pH 2.18. The formation of HCHO is a result of the ongoing oxidation of

methanol by ROS or h^+ , thus the yield of HCHO can serve as an indicator for assessing CH_3OH selectivity. The amount of HCHO was determined by the acetylacetone colorimetric method, measuring absorbance at 413 nm on a UV-vis spectrophotometer [27]. Additionally, potential gas products collected in the reactor, such as CO, CO_2 , and C_2H_6 were analyzed via the GC7900 with a TDX-1 column.

2.5. The detection of radicals

The samples were dispersed in water using 5,5-dimethyl-1-pyrroline-N-oxide (DMPO) as the radicals trapping agent to detect hydroxyl radicals ($\bullet\text{OH}$) and methyl radicals ($\bullet\text{CH}_3$), as well as in methanol to detect superoxide radicals ($\bullet\text{O}_2^-$). In detail, the catalysts were dispersed in water or methanol (0.5 g/L) with CH_4/N_2 or N_2 bubbling, and the suspension was prepared by adding a specific amount of H_2O_2 or introducing O_2 as appropriate. 50 μL above suspension was mixed with 5 μL DMPO to obtain the final mixture. After being in situ light, the mixture was characterized using the EPR spectrometer at room temperature.

3. Results and discussion

3.1. Characterization

In Fig. 1a, the XRD pattern of the Fe-BTC was in excellent agreement with the simulated pattern. Notably, no discernible diffraction peaks corresponding to the PTA crystals were observed in the PWFe-2, indicating that the PTA clusters were mainly encapsulated within the cages of Fe-BTC. In the range of 5.0°–8.0°, Fe-BTC exhibited characteristic peaks, while PWFe-2 only showed an insignificant broad peak. It could be attributed to the interaction between PTA and Fe-BTC, which altered the crystal structure of Fe-BTC and resulted in changes in electron density [28]. The morphology and dimensions of the synthesized composites were analyzed by means of scanning electron microscopy (SEM). The morphology of the Fe-BTC remained unchanged with the presence of PTA, revealing an octahedral shape, indicating that PTA did not aggregate on the surface, and the particle size ranged from 200 to 500 nm, as depicted in Fig. S1.

The IR spectra of PWFe-X exhibited characteristic peaks of both Fe-BTC and PTA, indicating the successful incorporation of PTA (Fig. 1b).

Table 1

The BET surface areas and total pore volumes of the samples.

Catalyst	BET surface area ($\text{m}^2 \cdot \text{g}^{-1}$)	Total pore volume ($\text{cm}^3 \cdot \text{g}^{-1}$)
Fe-BTC	858.10	0.45
PWFe-1	583.57	0.36
PWFe-2	371.33	0.20
PWFe-3	197.26	0.13

The peaks at 1625, 1448, and 1380 cm^{-1} were assigned to carboxylate C=O stretching vibrations, as well as symmetric and asymmetric vibrations of the COO⁻ group. Additionally, the bands around 758 and 711 cm^{-1} were ascribed to C-H vibrations within the benzene ring. The band observed at 626 cm^{-1} corresponded to the Fe–O tensile vibration, providing evidence for the presence of iron in the framework. These results confirmed the successful formation of acid-organic bonds and metal ions within the Fe-BTC [29]. PTA exhibited four characteristic peaks, among which the absorption band at 1080 cm^{-1} was attributed to the asymmetric stretching vibration of the P-O bond in tetrahedral PO₄. The peak at 984 cm^{-1} corresponded to the W=O vibration of the terminal. The vibrational modes at 893 cm^{-1} and 802 cm^{-1} were classified as W-O_b-W and W-O_c-W, respectively [30]. The characteristic vibration of PTA in PWFe-X was slightly altered compared to pure PTA, possibly due to the confinement effect of the Fe-BTC cage on PTA clusters [26]. The Raman spectra detection yielded analogous evidence, as detailed in Fig. S2. Briefly, the bands at 810 and 1004 cm^{-1} belonged to the benzene ring vibration of H₃BTC [29]. After the introduction of PTA, it was evident that the band at 1004 cm^{-1} significantly widens, possibly due to the presence of the W=O bond. With increasing amounts of PTA, a new peak emerged at 910 cm^{-1} , which might be attributed to the vibration of W-O-W [31].

The position of PTA in Fe-BTC was further investigated through N₂ adsorption-desorption experiments at 77 K. Fig. 1e displayed the I-type nitrogen adsorption-desorption curves of the prepared samples, and the desorption curves exhibited a certain degree of hysteresis, which might be attributed to the swelling effect in liquid nitrogen [32]. Detailed results indicated that both BET specific surface area and total pore volume decreased with the increase of PTA introduction (Table 1). This was because PTA partially occupied the Fe-BTC cavity, leading to a reduction in its N₂ adsorption capacity [33]. The pore size distribution (PSD) in the material was analyzed using the density functional theory (DFT) model. It was evident that the volume of micropores in the material significantly decreased after PTA immobilization compared to pure MOFs, further indicating that the PTA were located in the small channels (Fig. S3).

XPS measurements were conducted to determine the elemental composition and chemical states of the PWFe-2 sample. The survey spectrum exhibited characteristic peaks of P 2p, W 4f, Fe 2p, O 1s, and C 1s (Fig. S4a). Further, the C 1s spectrum could be resolved into two distinct peaks located at 284.8 and 288.9 eV, corresponding to electron binding energies in the phenyl and carboxyl groups, respectively (Fig. S4b) [34]. The high-resolution Fe 2p spectrum displayed two fitted peaks at 711.9 and 725.5 eV with a difference of 13.6 eV, indicating the presence of Fe(III) (Fig. 1c). At the same time, phosphorus with a binding energy of 134.2 eV (P 2p) (Fig. S4c) and tungsten in high oxidation state with the binding energy of 35.8 (W 4f_{5/2}) and 37.9 eV (W 4f_{7/2}) were detected (Fig. 1d), which were well consistent with the theoretical value of the keggin-type PTA structure [35].

The optical absorption capacity of the catalyst was investigated via UV-vis absorption spectroscopy (Fig. 1f). Fe-BTC exhibited a strong UV absorption with a maximum of around 300 nm, which might be attributed to the LMCT from O(II) to Fe(III). Additionally, the spin d-d transition of Fe(III) in MOFs [${}^6\text{A}_{1g} = {}^4\text{A}_{1g} + {}^4\text{E}_g$ (G)] could account for the band observed between 300 and 600 nm [36]. Following the introduction of PTA, the optical properties of Fe-BTC remained essentially unaltered, exhibiting only a slight increase in absorption intensity and a red shift of the absorption edge. Finally, the actual amount of PTA

Table 2

The ICP of fresh PWFe-2 and used PWFe-2.

Catalyst	Metallic element	wt%	n (PW ₁₂) / n (Fe species)
Fresh PWFe-2	W / Fe	35.31 / 10.76	1.77 / 8.57 = 0.21
Used PWFe-2	W / Fe	38.59 / 11.99	2.29 / 11.28 = 0.20

immobilized was determined through ICP-OES, and the results indicated that they were in close agreement with theoretical values (Table 2).

3.2. Performance experiments

3.2.1. Exploration of the photoexcitation process

POMs can capture photoelectrons during photoexcitation, and the resulting reduced species exhibit a dark blue coloration known as heteropoly blues (HPBs), with a characteristic absorption band in the visible region (Fig. 2a-b) [37,38]. The subsequent inquiry pertained to the potential of PTA encapsulated within MOFs to undergo a state of reduction through stored photoelectrons following irradiation. After in situ irradiation, the UV-vis absorption curves of the solution of the PTA-containing catalyst showed a significant upward shift in the visible region (Fig. 2c) [39]. Additionally, XPS analysis revealed a substantial decrease in the binding energy of W, in contrast to the binding energy of O remained unchanged (Fig. S5a-b). The O 1s peak at 531.7 eV was attributed to oxygen atoms within carboxylic acid groups of the H₃BTC linker present in Fe-BTC [40]. These findings suggested that the PTA exhibited self-reducing electron storage behavior within MOFs.

Recent theoretical developments have unveiled the potential transfer of photoelectrons from POMs to MOFs through hydrogen bonding interactions, thereby enabling metal sites to acquire electrons and reduce their chemical valence [25,41]. Photoluminescence experiments were utilized to investigate the migration and recombination processes of photogenerated electron-hole pairs. As shown in Fig. S6a, pure MOFs exhibited a higher intensity of fluorescence absorption peak than the composites, indicating the electron transfer interaction between the introduced PTA and Fe-BTC framework [42]. The higher photocurrent response observed in the composites compared to pure MOFs confirmed that the former exhibited enhanced carrier generation and separation (Fig. S6b). These two tests confirmed the occurrence of charge transfer between PTA and Fe-BTC. The solid-state EPR measurements revealed a significant weakening of the characteristic peak of Fe(III) in the octahedral FeO₆ coordination environment of the catalyst after irradiation in an aqueous solution, indicating a shift to a lower valence state due to the absence of a strongly oxidizing environment (Fig. 2d) [36,43]. In addition, XPS analysis similarly revealed a decrease in the Fe binding energy before and after light exposure to the material (Fig. S7). Hence, the metal sites within the MOFs could also be considered units for storing electrons (Eq. 4).



3.2.2. Performance experiments

Reduced POMs can revert to POMs under non-light conditions in the presence of electron sacrificial agents such as O₂ or H₂O₂, thus constituting a redox cycle and simultaneous release of ROS, which can drive the oxidation of CH₄ (Eqs. 5–6). From that characteristic, we found that the catalyst would store more photoelectrons as the excitation light wavelength decreases, resulting in a significant enhancement of CH₄ to CH₃OH conversion efficiency when utilizing H₂O₂ as an oxidant in the dark (Fig. 3a). Meanwhile, CH₃OH could also be produced from O₂ was employed as an oxidant during dark conditions, but selectivity remained difficult to guarantee (Fig. S8). This phenomenon could be attributed to the fact that •OH generated from H₂O₂ cleavage exhibited milder reactivity in the DCMM reaction, which could be more effectively

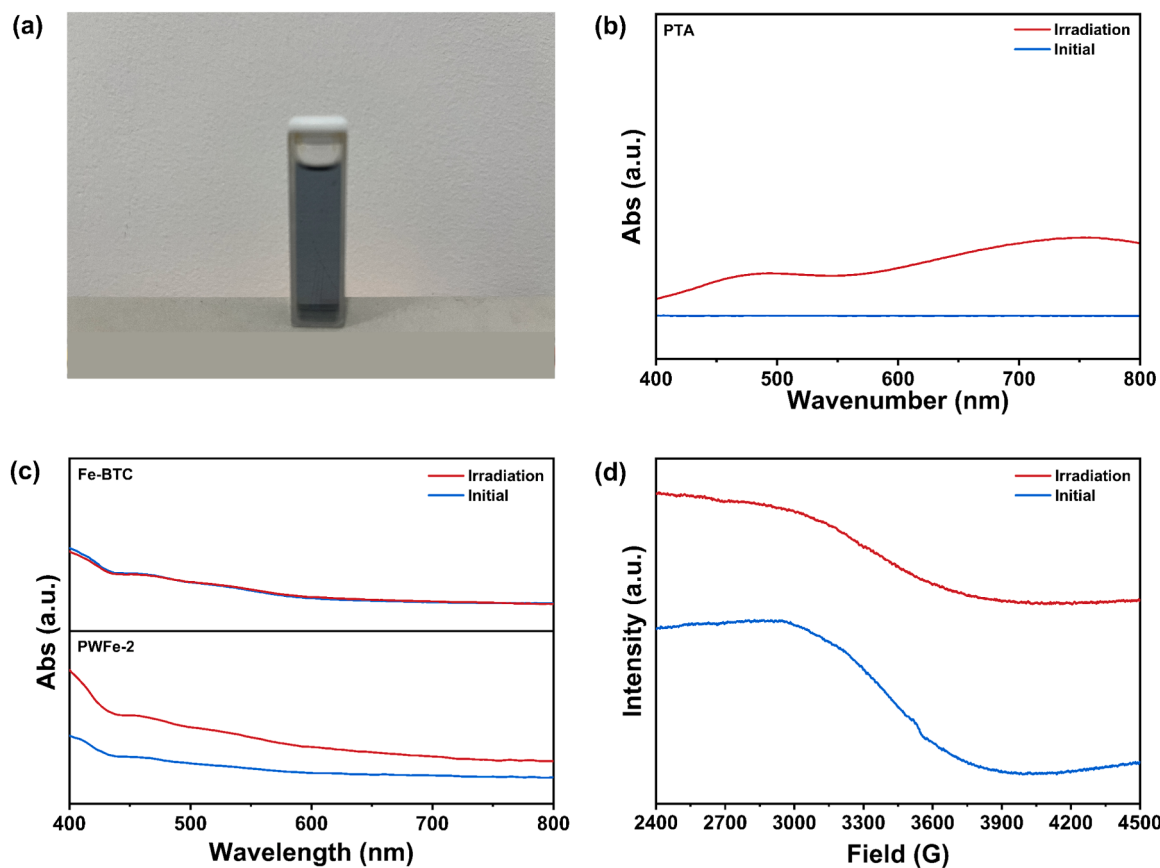
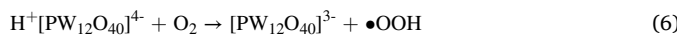
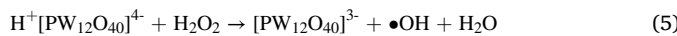


Fig. 2. (a) Dark blue self-reduced phosphotungstic acid. UV–vis absorbance spectra of (b) PTA, (c) Fe-BTC and PWFe-2 aqueous solution in the dark (initial) and after light exposure for 30 min (irradiation). (d) The EPR spectra of Fe(III) in PWFe-2 before and after irradiation.

regulated through the catalyst, thereby promoting selectivity towards alcohols [44]. In contrast, a significant amount of HCHO generated was detected due to the overoxidation tendency of $\bullet\text{O}_2$ produced after activation of O_2 , which was consistent with previously reported findings [45]. In addition, the simultaneous introduction of both oxidants into the dark reaction likewise led to an increase in HCHO yield, as previous studies had suggested that the re-oxidation kinetics of POM_{red} was slower in the presence of H_2O_2 than O_2 , which might result in a potential rise in $\bullet\text{O}_2$ radicals (Fig. S9) [37].



However, the synthesized PWFe-2 was utilized in the conventional photocatalytic process, the CH_4 conversion rate showed a gradual enhancement with the decrease in excitation light wavelength during H_2O_2 oxidation, while the overoxidation of the product CH_3OH was promoted, resulting in an unsatisfactory yield (Fig. 3b). When O_2 was employed as the oxidant, none of the alcohol products were detected. The statement further corroborated the theoretical conjecture and underscored the superiority of the modified catalytic strategy.

3.2.3. Control experiments and stability tests

A series of blank experiments demonstrated that the absence of the catalyst, methane, or oxidant resulted in no methanol production (Fig. S10). While trace amounts of methanol were detected in the pure dark reaction, this might be attributed to the action of water-soluble CH_4 and $\bullet\text{OH}$ produced by the Fenton-like reaction of iron species with H_2O_2 . In conclusion, the high yields of liquid oxygenated compounds were formed through CH_4 oxidation via dark photocatalysis in the presence of relevant catalysts.

In order to achieve optimal CH_3OH yield, the influence of relevant parameters on experimental performance was investigated. (i) The relationship between product yield and the amount of PTA introduction followed a "volcano-type" trend, where an increase in the latter resulted in higher reaction activity. However, excessive encapsulation led to MOFs' pore blockage, thereby reducing the performance (Fig. 3c). (ii) With an increase in the catalyst dosage, the number of stored photoelectrons also increased, resulting in a corresponding improvement in reaction performance. However, continued dosage escalation would inevitably lead to a masking effect between particles, rendering the improvement in reaction performance indiscernible beyond a certain dosage (Fig. S11a) [46]. This critical dosage ensured full absorption of catalyst particles under light irradiation. (iii) Due to the rapid diffusion of H_2O_2 from the active site, the concentration of H_2O_2 was directly related to the yield of ROS and thus significantly impacted CH_3OH yield [47]. As the concentration increased, the harmful attack of ROS on CH_3OH gradually intensified, leading to a decrease in selectivity (Fig. S11b). (iv) Since the total number of electrons involved in photo-electron formation was fixed, the number of photoelectrons decreased continuously over reaction time as they were consumed. Similarly, the extent of overoxidation gradually intensified with an increase in ROS concentration (Fig. S11c). On this basis, optimal reaction parameters facilitated the achievement of CH_3OH yields up to $968 \mu\text{mol}\cdot\text{g}_{\text{cat}}^{-1}\cdot\text{h}^{-1}$ under ambient conditions.

Since the catalyst was composed of two distinct parts, each was tested separately for its catalytic performance to elucidate their respective roles. It was observed that the isolated Fe-BTC exhibited negligible produced CH_3OH , whereas a more visible performance was demonstrated when using pure PTA as a catalyst, corresponding to 103 and $474 \mu\text{mol}\cdot\text{g}_{\text{cat}}^{-1}\cdot\text{h}^{-1}$, respectively. This implied that the photocatalyst Fe-BTC lacks the ability to store photoelectrons, whereas PTA served as

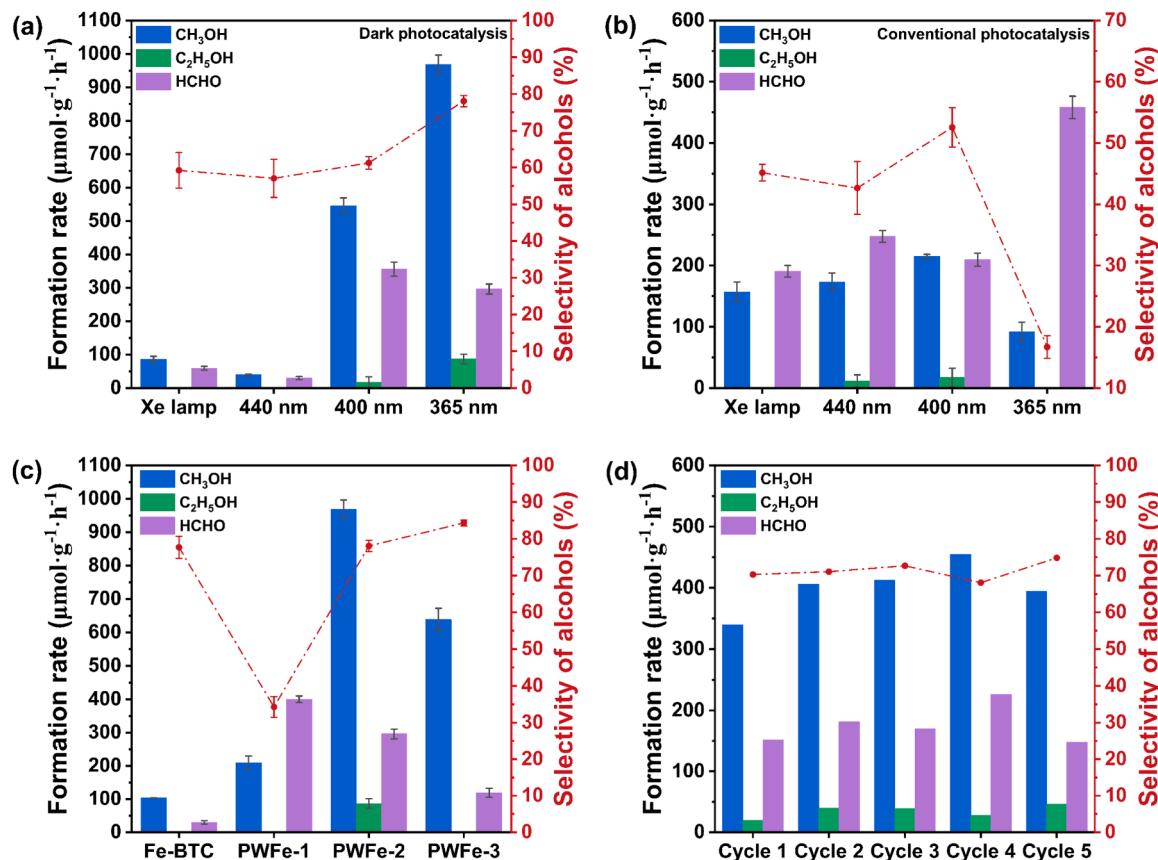


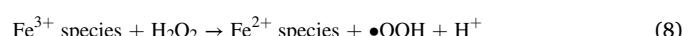
Fig. 3. Performances of catalytic methane to oxygenated products (such as CH_3OH , $\text{C}_2\text{H}_5\text{OH}$, and HCHO). The productivity under different irradiation light wavelengths in (a) the dark photocatalytic mode and (b) the conventional photocatalytic mode. Reaction parameters: 15 mg PWFe-2, 200 μL 30 % H_2O_2 , 300 W Xenon lamp ($\lambda > 420 \text{ nm}$). (c) The productivity under different PTA immobilized contents. Reaction parameters: 15 mg catalyst, 365 nm LED, 200 μL 30% H_2O_2 . (d) Cycling tests of the catalyst. Reaction parameter: 30 mg PWFe-2, 365 nm LED, 200 μL 30% H_2O_2 . Error bars represent the standard deviations of at least three repeated experiments under the same conditions.

the primary reaction center in the composite. The physical mixture feeds were inferior to the composites, corresponding to 441 and 968 $\mu\text{mol}\cdot\text{g}^{-1}\cdot\text{h}^{-1}$, respectively, indicating the crucial role of shell Fe-BTC for gas enrichment (Fig. S11d). It was evident that the effective combination of both components to form a unified catalyst would enhance their synergy, resulting in a reaction performance higher than the sum of its parts.

Furthermore, the reaction activity remained constant throughout the cycling process (Fig. 3d), as evidenced by the unaltered XRD pattern of the recovered catalyst, indicating its stability (Fig. 1a). In conjunction with IR spectra of the recovered catalyst (Fig. S12) and ICP-OES test data (Table 2), they provided additional evidence that there was no leaching of PTA during the reaction. Meanwhile, the absence of CO or CO_2 in the gaseous by-products as well as traces of HCOOH (further oxidation products of HCHO) was detected, indicating the effective suppression of methane overoxidation within this system. The pH value of the filtrate, monitored at the end of each experimental round, remained consistent with its pre-experimental level. This observation further ruled out the possibility that the introduced PTA was dislodged from the frameworks and that the significant amount of CO_2 produced during the reaction was dissolved in water. Additionally, the catalyst underwent a one-week immersion in water, followed by an analysis of the resulting solution (the catalyst was removed) to detect any leaching of PTA. The UV-vis absorbance spectra of the solutions (Fig. S13) revealed no discernible features indicating the presence of PTA and negligible alteration in solution absorbance after irradiation, providing further evidence for efficient immobilization and stabilization of PTA within Fe-BTC.

3.3. Possible mechanism

The introduction of O_2 during light reactions led to a significant decrease in CH_3OH production performance attributed to the re-oxidation of reduced PTA, thus highlighting the critical role effective photoelectron storage played throughout the entire mechanism (Fig. S14). Intuitively, it was apparent that photoexcitation could improve the ability of the catalyst to activate $\bullet\text{OH}$ production from H_2O_2 . The EPR testing demonstrated a dramatical increase in the ability of the composite after exposure to light (Fig. 4a), while the pure Fe-BTC remained essentially at the same level (Eq. 7) (Fig. 4b). Furthermore, the Fe^{3+} present in the catalyst also underwent a Fenton-like reaction with H_2O_2 , resulting in the generation of $\bullet\text{OOH}$ radicals (Eq. 8) (Fig. S15) [48]. Experiments on quenching of reactive species had demonstrated that the addition of isopropanol (IPA), which acted as a $\bullet\text{OH}$ quencher, inhibited the formation of CH_3OH and HCHO in the dark reaction. It suggested that $\bullet\text{OH}$ radicals play a dominant role in CH_4 conversion during this route (Fig. S14).



In addition, literature reports suggest that anionic groups with an electron-rich environment in PTA can stabilize the methyl group through electrostatic interactions. It forms a relatively stable POM- CH_3 species, where the methyl group is attached to the terminal oxygen site of POMs [49]. As a result, successive dehydrogenation of methane is

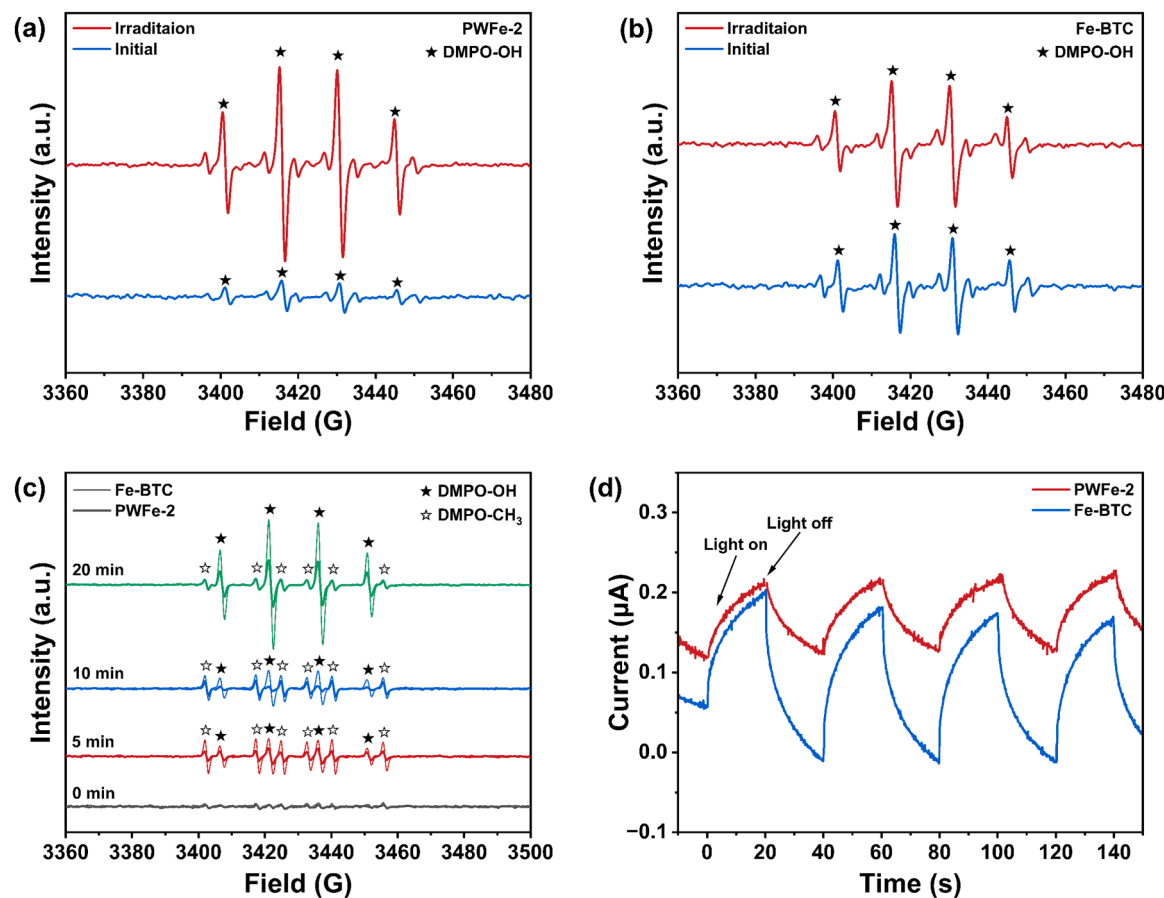


Fig. 4. The EPR spectra of DMPO-OH adducts produced by the interaction of (a) PWFe-2 or (b) Fe-BTC with H₂O₂. (c) The EPR spectra of DMPO-OH and DMPO-CH₃ adduct were observed in an aqueous solution in the presence of methane and Fe-BTC or PWFe-2 after in situ irradiation. (d) The difference in photocurrent responses of Fe-BTC and PWFe-2 before and after adding 10 wt% of CH₃OH to the electrolyte solution.

avoided. We substantiated the point above via EPR. It was well known •OH could abstract hydrogen from CH₄ to generate •CH₃, which promptly combined with •OH under constant illumination, rendering it indiscernible in measurements. Due to longer lifetimes of DMPO-CH₃ than DMPO-OH, the signal of the latter gradually weakened in the dark after a certain time (exceeding the DMPO-OH lifetime) of in situ light exposure while the former slowly strengthened. On this basis, when PTA was dissolved in an aqueous solution with CH₄, the •OH signal was found to decrease with increasing light time (within the DMPO-OH lifetime), indicating further interaction between PTA and •OH radical, which would be described in detail subsequently. However, no significant •CH₃ signal could be detected, suggesting that the intermediate methyl group might be stabilized by PTA (Fig. S16a) [50]. In contrast, the presence of shell Fe-BTC mitigated the interaction between PTA and the methyl group, thereby enabling the detection of •CH₃ signal in the composite (Fig. S16b). At the same time, no •CH₃ signal was produced in the aqueous solution without CH₄ (Fig. S16c).

Finally, although the transformation of the reaction mode could significantly improve CH₃OH product selectivity, the presence of •OH in the dark reaction still promoted the conversion of CH₃OH. Therefore, we also investigated how material properties themselves could inhibit this aspect. Specifically, conducting the aforementioned EPR measurements method (in situ light followed by testing in the dark), it was observed that both Fe-BTC and PWFe-2 exhibited significant •CH₃ and •OH signals. In the liquid phase system, •OH radicals in the bulk phase exhibited a higher propensity to activate CH₄ than those bound at the surface because methane was less soluble and more challenging to adsorb to the catalyst surface, rendering free CH₄ molecules more susceptible to overoxidation. Conversely, the surface-bound •OH facilitated •CH₃

binding for CH₃OH formation, reducing the probability of interaction with the product [51]. Thereby explaining why both •CH₃ and •OH signals were stronger in the pure MOFs system than in the composite, possibly due to the presence of PTA enhancing the adsorption of •OH, which was intrinsic to the ability of PWFe-2 system to inhibit CH₃OH overoxidation (Fig. 4c) [52]. Moreover, in order to evaluate the intrinsic oxidation performance of the catalyst for methanol, 10 wt% of CH₃OH was added to the electrolyte solution required for photocurrent testing. The addition of the hole sacrificial agent must result in an enhanced photocurrent signal, and the difference between signals before and after its introduction was compared. The smaller difference observed for the composite indicated a preference for stabilizing the target product CH₃OH (Fig. 4d) [53].

In summary, a plausible reaction mechanism was introduced: the encapsulated PTA underwent self-reduction under UV irradiation in an oxygen-free aqueous solution to form HPBs (Eqs. 1–3), which generated charge transfer with Fe-BTC and led to an increase of iron divalent sites (Eq. 4). In the subsequent dark reaction, CH₄ was introduced, and H₂O₂ was added, the latter interacted with the HPBs to generate •OH radicals and restored PTA (Eq. 5). Additionally, the Fenton-like reaction between iron sites on the MOFs and H₂O₂ promoted •OH radical generation while also producing some •OOH radicals (Eqs. 7–8). The •OH radicals reacted with CH₄ to abstract hydrogen, thus producing •CH₃ radicals, and the two radicals combined to form CH₃OH (Eqs. 10–11). Despite the presence of excess •OH and some •OOH radicals allowing further overoxidation of CH₃OH to HCHO (Eqs. 12–16), it was not negatively affected by photoexcitation during CH₃OH production and effective limitation of non-selective oxidation of •OH radicals by PTA introduced in the composites, as well as an increased reaction barrier for CH₃OH

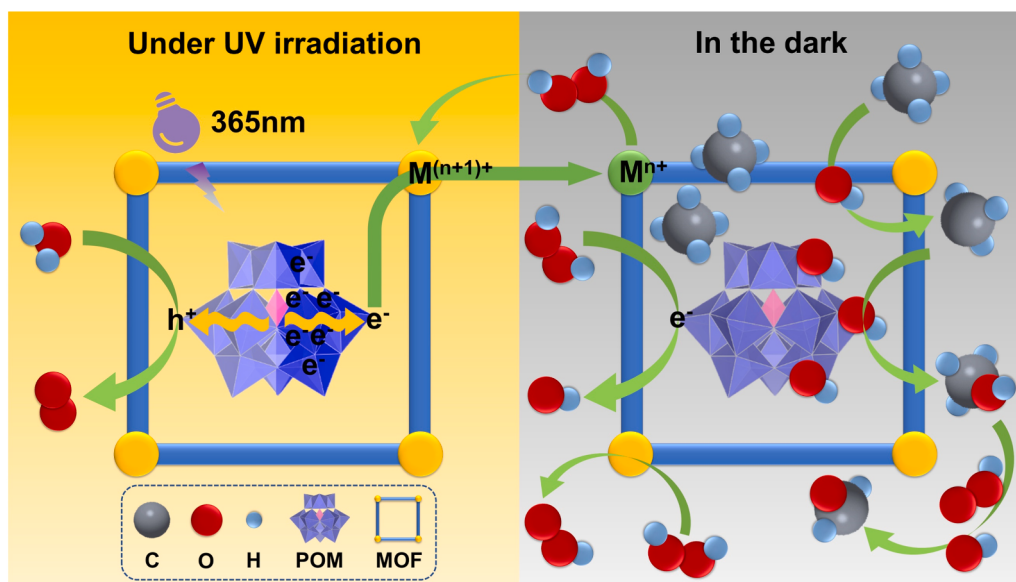
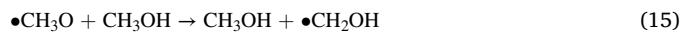


Fig. 5. Proposed schematic mechanism for selective oxidation of methane via dark photocatalysis.

under mild conditions (Fig. 5). These factors collectively facilitated the reaction process of partial oxidation of CH_4 to CH_3OH . It was worth noting that during the further attack of the $\bullet\text{OH}$ on the CH_3OH , the resulting free radicals might be coupled, resulting in the formation of $\text{C}_2\text{H}_5\text{OH}$ (Eqs. 17–18). Furthermore, there was also a significant enhancing the performance of other catalysts with similar composition (such as STA/Fe-BTC and PTA/Cu-BTC), thus demonstrating the universality of the overall idea (Fig. S17).



4. Conclusion

In conclusion, the mode of dark photocatalysis circumvented the deleterious side reactions of photogenerated holes for alcohols and mitigated the inefficacious oxygen evolution reaction occurring in hydrogen peroxide degradation. Systematic experiments and related characterization demonstrated that the PTA encapsulated in Fe-BTC stored the photogenerated electrons produced under UV light, while interacting with hydrogen peroxide in the dark to generate hydroxyl radicals, which participated in hydrogen abstraction to initiate methane conversion. Apart from the gas enrichment function, the iron sites on the Fe-BTC also participated in the Fenton-like reaction with hydrogen peroxide, which further accelerated methane conversion. Meanwhile, the introduction of PTA could stabilize the methyl intermediate and effectively regulate the hydroxyl radical, thereby weakening its further reaction with methanol. The optimal experimental parameters achieved methanol yields up to $968 \mu\text{mol}\cdot\text{g}_{\text{cat}}^{-1}\cdot\text{h}^{-1}$ under ambient conditions. In

addition, this changed reaction mode was transferable to other similar composites. This work presented a new idea for the direct and efficient conversion of inert methane to methanol, which expanded the scope of related research topics.

CRediT authorship contribution statement

Taikang Jia and Wenjing Wang: Investigation, Methodology, Validation, Formal analysis, Writing - Original Draft. **Ling Zhang:** Conceptualization, Supervision, Funding acquisition. **Di Zeng:** Investigation, Formal analysis. **Juxue Wang:** Validation, Formal analysis. **Wenzhong Wang:** Conceptualization, Supervision, Funding acquisition.

Declaration of Competing Interest

The authors declare that they have no known competing financial interests or personal relationships that could have appeared to influence the work reported in this paper.

Data availability

Data will be made available on request.

Acknowledgment

This work was financially supported by the National Natural Science Foundation of China (51972325, 52172256, 51972327).

Supporting Information

Supporting information, including Fig. S1~S17 related to this article, can be found in the online version.

Author Contributions

Wenzhong Wang and Ling Zhang conceived the idea and supervised the whole project. Taikang Jia and Wenjing Wang designed and carried out all the experiments. Di Zeng and Juxue Wang contributed to analysis of mechanism. All the authors contributed to writing the manuscript and approved the final version of the manuscript for submission.

Notes

The authors declare no competing financial interest.

Appendix A. Supporting information

Supplementary data associated with this article can be found in the online version at [doi:10.1016/j.apcatb.2023.123168](https://doi.org/10.1016/j.apcatb.2023.123168).

References

- [1] E.G. Nisbet, E.J. Dlugokencky, P. Bousquet, Atmospheric science. Methane on the rise—again, *Science* 343 (2014) 493–495, <https://doi.org/10.1126/science.1247828>.
- [2] E. McFarland, Chemistry. Unconventional chemistry for unconventional natural gas, *Science* 338 (2012) 340–342, <https://doi.org/10.1126/science.1226840>.
- [3] Y.D. Xu, X.H. Bao, L.W. Lin, Direct conversion of methane under nonoxidative conditions, *J. Catal.* 216 (2003) 386–395, [https://doi.org/10.1016/S0021-9517\(02\)00124-0](https://doi.org/10.1016/S0021-9517(02)00124-0).
- [4] G.A. Olah, Beyond oil and gas: the methanol economy, *Angew. Chem. Int. Ed. Engl.* 44 (2005) 2636–2639, <https://doi.org/10.1002/anie.200462121>.
- [5] H. Song, X.G. Meng, S.Y. Wang, W. Zhou, S. Song, T. Kako, J.H. Ye, Selective photo-oxidation of methane to methanol with oxygen over dual-cocatalyst-modified titanium dioxide, *ACS Catal.* 10 (2020) 14318–14326, <https://doi.org/10.1021/acscatal.0c04329>.
- [6] G.Q. Fang, J. Lin, X.D. Wang, Low-temperature conversion of methane to oxygenates by supported metal catalysts: from nanoparticles to single atoms, *Chin. J. Chem. Eng.* 38 (2021) 18–29, <https://doi.org/10.1016/j.cjche.2021.04.034>.
- [7] A.A. Latimer, A. Kakakhani, A.R. Kulkarni, J.K. Norskov, Direct methane to methanol: the selectivity-conversion limit and design strategies, *ACS Catal.* 8 (2018) 6894–6907, <https://doi.org/10.1021/acscatal.8b00220>.
- [8] X. Meng, X. Cui, N.P. Rajan, L. Yu, D. Deng, X. Bao, Direct methane conversion under mild condition by thermo-, electro-, or photocatalysis, *Chem* 5 (2019) 2296–2325, <https://doi.org/10.1016/j.chempr.2019.05.008>.
- [9] H. Song, X.G. Meng, Z.J. Wang, H.M. Liu, J.H. Ye, Solar-energy-mediated methane conversion, *Joule* 3 (2019) 1606–1636, <https://doi.org/10.1016/j.joule.2019.06.023>.
- [10] Y. Tang, Y. Li, F. Feng Tao, Activation and catalytic transformation of methane under mild conditions, *Chem. Soc. Rev.* 51 (2022) 376–423, <https://doi.org/10.1039/d1cs00783a>.
- [11] S.Y. Fang, Y.H. Hu, Thermo-photo catalysis: a whole greater than the sum of its parts, *Chem. Soc. Rev.* 51 (2022) 3609–3647, <https://doi.org/10.1039/d1cs00782c>.
- [12] H. Song, X. Meng, S. Wang, W. Zhou, X. Wang, T. Kako, J. Ye, Direct and selective photocatalytic oxidation of CH₄ to oxygenates with O₂ on cocatalysts/ZnO at room temperature in water, *J. Am. Chem. Soc.* 141 (2019) 20507–20515, <https://doi.org/10.1021/jacs.9b11440>.
- [13] Y. Nosaka, A.Y. Nosaka, Generation and detection of reactive oxygen species in photocatalysis, *Chem. Rev.* 117 (2017) 11302–11336, <https://doi.org/10.1021/acs.chemrev.7b00161>.
- [14] X.Y. Li, C. Wang, J.W. Tang, Methane transformation by photocatalysis, *Nat. Rev. Mater.* 7 (2022) 617–632, <https://doi.org/10.1038/s41578-022-00422-3>.
- [15] M. Huang, S. Zhang, B. Wu, Y. Wei, X. Yu, Y. Gan, T. Lin, F. Yu, F. Sun, Z. Jiang, Selective photocatalytic oxidation of methane to oxygenates over Cu–W–TiO₂ with significant carrier traps, *ACS Catal.* 12 (2022) 9515–9525, <https://doi.org/10.1021/acscatal.2c02424>.
- [16] A. Hameed, I.M.I. Ismail, M. Aslam, M.A. Gondal, Photocatalytic conversion of methane into methanol: performance of silver impregnated WO₃, *Appl. Catal. A-Gen.* 470 (2014) 327–335, <https://doi.org/10.1016/j.apcata.2013.10.045>.
- [17] Y.T. Pan, J.X. Wang, S.Y. Chen, W.J. Yang, C.M. Ding, A. Waseem, H.L. Jiang, Linker engineering in metal–organic frameworks for dark photocatalysis, *Chem. Sci.* 13 (2022) 6696–6703, <https://doi.org/10.1039/D1SC06785K>.
- [18] S.M. Qiao, Y.Y. Zhou, H.C. Hao, X.C. Liu, L. Zhang, W.Z. Wang, Selective hydrogenation via cascade catalysis on amorphous TiO₂, *Green Chem.* 21 (2019) 6585–6589, <https://doi.org/10.1039/c9gc03019k>.
- [19] T. Imyen, E. Znoutine, D. Suttipat, P. Iadrat, P. Kidkhunthod, S. Bureekaew, C. Wattanakit, Methane utilization to methanol by a hybrid zeolite@metal–organic framework, *ACS Appl. Mater. Interfaces* 12 (2020) 23812–23821, <https://doi.org/10.1021/acsmami.0c02273>.
- [20] A.M. Chávez, A. Rey, J. López, P.M. Álvarez, F.J. Beltrán, Critical aspects of the stability and catalytic activity of MIL-100(Fe) in different advanced oxidation processes, *Sep. Purif. Technol.* 255 (2021), 117660, <https://doi.org/10.1016/j.seppur.2020.117660>.
- [21] M. Zhang, H.J. Li, J.H. Zhang, H.J. Lv, G.Y. Yang, Research advances of light-driven hydrogen evolution using polyoxometalate-based catalysts, *Chin. J. Catal.* 42 (2021) 855–871, [https://doi.org/10.1016/S1872-2067\(20\)63714-7](https://doi.org/10.1016/S1872-2067(20)63714-7).
- [22] S. Amthor, S. Knoll, M. Heiland, L. Zedler, C.Y. Li, D. Nauroozi, W. Tobaschus, A. K. Mengelle, M. Anjass, U.S. Schubert, B. Dietzek-Ivancic, S. Rau, C. Streb, A photosensitizer-polyoxometalate dyad that enables the decoupling of light and dark reactions for delayed on-demand solar hydrogen production, *Nat. Chem.* 14 (2022) 321–327, <https://doi.org/10.1038/s41557-021-00850-8>.
- [23] J.M. Sun, S. Abednatanzi, P. Van Der Voort, Y.Y. Liu, K. Leus, POM@MOF hybrids: synthesis and applications, *Catalysts* 10 (2020) 578, <https://doi.org/10.3390/catal10050578>.
- [24] X.S. Wang, L. Li, J. Liang, Y.B. Huang, R. Cao, Boosting oxidative desulfurization of model and real gasoline over phosphotungstic acid encapsulated in metal–organic frameworks: the window size matters, *ChemCatChem* 9 (2017) 971–979, <https://doi.org/10.1002/cctc.201601450>.
- [25] M.L. Yang, X.M. Wang, C.J. Gomez-Garcia, Z.X. Jin, J.J. Xin, X.X. Cao, H.Y. Ma, H. J. Pang, L.C. Tan, G.X. Yang, Y.H. Kan, Efficient electron transfer from an electron-reservoir polyoxometalate to dual-metal-site metal–organic frameworks for highly efficient electroreduction of nitrogen, *Adv. Funct. Mater.* (2023), 2214495, <https://doi.org/10.1002/adfm.202214495>.
- [26] R.W. Liang, R.K. Huang, S.M. Ying, X.X. Wang, G.Y. Yan, L. Wu, Facile in situ growth of highly dispersed palladium on phosphotungstic-acid-encapsulated MIL-100(Fe) for the degradation of pharmaceuticals and personal care products under visible light, *Nano Res.* 11 (2018) 1109–1123, <https://doi.org/10.1007/s12274-017-1730-0>.
- [27] Y. Jiang, W. Zhao, S. Li, S. Wang, Y. Fan, F. Wang, X. Qiu, Y. Zhu, Y. Zhang, C. Long, Z. Tang, Elevating photooxidation of methane to formaldehyde via TiO₂ crystal phase engineering, *J. Am. Chem. Soc.* 144 (2022) 15977–15987, <https://doi.org/10.1021/jacs.2c04884>.
- [28] Z. Zhang, J. Ren, J. Xu, L. Meng, P. Zhao, Z. Wang, Long-term durable solid state electrolyte membranes based on a metal–organic framework with phosphotungstic acid confined in the mesoporous cages, *Int. J. Hydrog. Energy* 45 (2020) 27527–27538, <https://doi.org/10.1016/j.ijhydene.2020.07.024>.
- [29] B.T. Le, D.D. La, P.T.H. Nguyen, Ultrasonic-assisted fabrication of MIL-100(Fe) metal–organic frameworks as a carrier for the controlled delivery of the chloroquine drug, *ACS Omega* 8 (2023) 1262–1270, <https://doi.org/10.1021/acsomega.2c06676>.
- [30] S. Ribeiro, A.D.S. Barbosa, A.C. Gomes, M. Pillinger, I.S. Goncalves, L. Cunha-Silva, S.S. Balula, Catalytic oxidative desulfurization systems based on Keggin phosphotungstate and metal–organic framework MIL-101, *Fuel Process. Technol.* 116 (2013) 350–357, <https://doi.org/10.1016/j.fuproc.2013.07.011>.
- [31] Y.Y. Zhang, C. Li, Z.T. Du, X. Chen, C.H. Liang, Dehydration of sorbitol into isosorbide over silver-exchanged phosphotungstic acid catalysts, *Mol. Catal.* 458 (2018) 19–24, <https://doi.org/10.1016/j.mcat.2018.08.005>.
- [32] S. Wu, Y. Liu, G. Yu, J. Guan, C. Pan, Y. Du, X. Xiong, Z. Wang, Facile preparation of dibenzoheterocycle-functional nanoporous polymeric networks with high gas uptake capacities, *Macromolecules* 47 (2014) 2875–2882, <https://doi.org/10.1021/ma500080s>.
- [33] S.D. Su, X.M. Li, X. Zhang, J.T. Zhu, G.D. Liu, M.Y. Tan, Y.Y. Wang, M. Luo, Keggin-type SiW₁₂ encapsulated in MIL-101(Cr) as efficient heterogeneous photocatalysts for nitrogen fixation reaction, *J. Colloid Interf. Sci.* 621 (2022) 406–415, <https://doi.org/10.1016/j.jcis.2022.04.006>.
- [34] F.M. Zhang, Y. Jin, J. Shi, Y.J. Zhong, W.D. Zhu, M.S. El-Shall, Polyoxometalates confined in the mesoporous cages of metal–organic framework MIL-100(Fe): Efficient heterogeneous catalysts for esterification and acetalization reactions, *Chem. Eng. J.* 269 (2015) 236–244, <https://doi.org/10.1016/j.cej.2015.01.092>.
- [35] P.A. Jalil, M. Faiz, N. Tabet, N.M. Hamdan, Z. Hussain, A study of the stability of tungstophosphoric acid, H₃PW₁₂O₄₀, using synchrotron XPS, XANES, hexane cracking, XRD, and IR spectroscopy, *J. Catal.* 217 (2003) 292–297, [https://doi.org/10.1016/S0021-9517\(03\)00066-6](https://doi.org/10.1016/S0021-9517(03)00066-6).
- [36] L. Chen, X. Wang, Z. Rao, Z. Tang, Y. Wang, G. Shi, G. Lu, X. Xie, D. Chen, J. Sun, In-situ synthesis of Z-Scheme MIL-100(Fe)/α-Fe₂O₃ heterojunction for enhanced adsorption and Visible-light photocatalytic oxidation of O-xylene, *Chem. Eng. J.* 416 (2021), 129112, <https://doi.org/10.1016/j.cej.2021.129112>.
- [37] Z. Wang, H. Hojo, H. Einaga, One-step oxidation of benzene to phenol with H₃PW₁₂O₄₀ under photoirradiation: Effect of operating conditions, *Chem. Eng. J.* 427 (2022), 131369, <https://doi.org/10.1016/j.cej.2021.131369>.
- [38] Y.H. Guo, C.W. Hu, X.L. Wang, Y.H. Wang, E.B. Wang, Y.C. Zou, H. Ding, S.H. Feng, Microporous decatungstates: synthesis and photochemical behavior, *Chem. Mater.* 13 (2001) 4058–4064, <https://doi.org/10.1021/cm010211i>.
- [39] Q. Ruan, X. Xi, B. Yan, L. Kong, C. Jiang, J. Tang, Z. Sun, Stored photoelectrons in a faradaic junction for decoupled solar hydrogen production in the dark, *Chem* 9 (2023) 1–15, <https://doi.org/10.1016/j.chempr.2023.03.001>.
- [40] Z.W. Yang, X.Q. Xu, X.X. Liang, C. Lei, Y.L. Wei, P.Q. He, B.L. Lv, H.C. Ma, Z.Q. Lei, MIL-53(Fe)-graphene nanocomposites: efficient visible-light photocatalysts for the selective oxidation of alcohols, *Appl. Catal. B-Environ.* 198 (2016) 112–123, <https://doi.org/10.1016/j.apcatb.2016.05.041>.
- [41] J.W. Jordan, A.I. Chernov, G.A. Rance, E. Stephen Davies, A.E. Lanterna, J. Alves Fernandes, A. Gruneis, Q. Ramasse, G.N. Newton, A.N. Khlobystov, Host-guest chemistry in boron nitride nanotubes: interactions with polyoxometalates and mechanism of encapsulation, *J. Am. Chem. Soc.* 145 (2023) 1206–1215, <https://doi.org/10.1021/jacs.2c10961>.
- [42] J. Du, Y.Y. Ma, W.J. Cui, S.M. Zhang, Z.G. Han, R.H. Li, X.Q. Han, W. Guan, Y. H. Wang, Y.Q. Li, Y. Liu, F.Y. Yu, K.Q. Wei, H.Q. Tan, Z.H. Kang, Y.G. Li, Unraveling photocatalytic electron transfer mechanism in polyoxometalate-encapsulated metal–organic frameworks for high-efficient CO₂ reduction reaction, *Appl. Catal. B-Environ.* 318 (2022), 121812, <https://doi.org/10.1016/j.apcatb.2022.121812>.
- [43] C. Xu, Y. Pan, G. Wan, H. Liu, L. Wang, H. Zhou, S.H. Yu, H.L. Jiang, Turning on visible-light photocatalytic C–H oxidation over metal–organic frameworks by introducing metal-to-cluster charge transfer, *J. Am. Chem. Soc.* 141 (2019) 19110–19117, <https://doi.org/10.1021/jacs.9b09954>.
- [44] Y. Jiang, S. Li, S. Wang, Y. Zhang, C. Long, J. Xie, X. Fan, W. Zhao, P. Xu, Y. Fan, C. Cui, Z. Tang, Enabling specific photocatalytic methane oxidation by controlling

free radical type, *J. Am. Chem. Soc.* 145 (2023) 2698–2707, <https://doi.org/10.1021/jacs.2c13313>.

[45] J.A. de Oliveira, J.C. da Cruz, O.R. Nascimento, C. Ribeiro, Selective CH₄ reform to methanol through partial oxidation over Bi₂O₃ at room temperature and pressure, *Appl. Catal. B-Environ.* 318 (2022), 121827, <https://doi.org/10.1016/j.apcatb.2022.121827>.

[46] P.M. Stanley, F. Sixt, J. Warnan, Decoupled solar energy storage and dark photocatalysis in a 3D metal-organic framework, *Adv. Mater.* 35 (2023), e2207280, <https://doi.org/10.1002/adma.202207280>.

[47] Z. Jin, L. Wang, E. Zuidema, K. Mondal, M. Zhang, J. Zhang, C. Wang, X. Meng, H. Yang, C. Mesters, F.S. Xiao, Hydrophobic zeolite modification for in situ peroxide formation in methane oxidation to methanol, *Science* 367 (2020) 193–197, <https://doi.org/10.1126/science.aaw1108>.

[48] R.W. Liang, S.G. Luo, F.F. Jing, L.J. Shen, N. Qin, L. Wu, A simple strategy for fabrication of Pd@MIL-100(Fe) nanocomposite as a visible-light-driven photocatalyst for the treatment of pharmaceuticals and personal care products (PPCPs), *Appl. Catal. B-Environ.* 176 (2015) 240–248, <https://doi.org/10.1016/j.apcatb.2015.04.009>.

[49] F. Lefebvre, Acid catalysis by heteropolyacids: transformations of alkanes, *Curr. Catal.* 6 (2017) 77–89, <https://doi.org/10.2174/221154470666170203123816>.

[50] P. Xie, J. Ding, Z. Yao, T. Pu, P. Zhang, Z. Huang, C. Wang, J. Zhang, N. Zecher-Freeman, H. Zong, D. Yuan, S. Deng, R. Shahbazian-Yassar, C. Wang, Oxo dicopper anchored on carbon nitride for selective oxidation of methane, *Nat. Commun.* 13 (2022) 1375, <https://doi.org/10.1038/s41467-022-28987-1>.

[51] Y.Y. Zhou, L. Zhang, W.Z. Wang, Direct functionalization of methane into ethanol over copper modified polymeric carbon nitride via photocatalysis, *Nat. Commun.* 10 (2019) 506, <https://doi.org/10.1038/s41467-019-08454-0>.

[52] H. Jin, P. Cui, C. Cao, X. Yu, R. Zhao, D. Ma, W. Song, Understanding the density-dependent activity of Cu single-atom catalyst in the benzene hydroxylation reaction, *ACS Catal.* 13 (2023) 1316–1325, <https://doi.org/10.1021/acscatal.2c05363>.

[53] C. Wang, X. Li, Y. Ren, H. Jiao, F.R. Wang, J. Tang, Synergy of Ag and AgBr in a pressurized flow reactor for selective photocatalytic oxidative coupling of methane, *ACS Catal.* 13 (2023) 3768–3774, <https://doi.org/10.1021/acscatal.2c06093>.